Multiscale Shear Impacts during the Genesis of Hagupit (2008)✐

CHAEHYEON C. NAM[a] AND MICHAEL M. BELL[a]

[a] *Colorado State University, Fort Collins, Colorado*

ABSTRACT: The impact of vertical wind shear (VWS) on tropical cyclogenesis is examined from the synoptic to meso-scales using airborne Doppler radar observations of predepression Hagupit during the Tropical Cyclone Structure 2008 (TCS08)/THORPEX Pacific Area Regional Campaign (T-PARC) field campaigns. The high temporal and spatial resolution observations reveal complex localized convective and vortical characteristics of a predepression in a sheared environment. Predepression Hagupit interacted with an upper-tropospheric trough during the observation period. The strong deep-layer VWS ($>20\,\mathrm{m\,s^{-1}}$) had a negative impact on the development through misalignment of the low- and midlevel circulations and dry air intrusion. However, the low-level circulation persisted, and the system ultimately formed into a tropical cyclone after it left the high-shear zone. Here we propose that a key process that enabled the predepression to survive through the upper-tropospheric trough interaction was persistent vorticity amplification on the meso-γ scale that was aggregated on the meso-α scale within the wave pouch. Multi-Doppler wind analysis indicates that cumulus congestus tilted the low-level horizontal vorticity into the vertical in the early stage of convective life cycle, followed by stretching from maturing deep convection. Variations in low-level VWS on the meso-β scale affect convective organization and horizontal vorticity generation. The results provide new insights into multiscale processes during TC genesis and the interactions of a predepression with VWS at various spatial scales.

KEYWORDS: Convective-scale processes; Cyclogenesis/cyclolysis; Wind shear; Hurricanes/typhoons; Radars/Radar observations

1. Introduction

Many researchers have studied tropical cyclone formation (i.e., tropical cyclogenesis) since the early 1900s (e.g., Weightman 1919). Over one century, researchers have made huge progress in our knowledge of tropical cyclogenesis, but many research questions still remain unanswered because of the complexity of the multiscale processes involved. The multiple spatiotemporal scales of dynamic and thermodynamic processes involved in tropical cyclogenesis range from large-scale ocean environments and background flows to convective-scale processes. One of the challenges to investigate these multiscale interactions is that high-resolution observations in a pregenesis storm are scarce. During the Tropical Cyclone Structure 2008 (TCS08) and THORPEX Pacific Area Regional Campaign (T-PARC) field experiments (Elsberry and Harr 2008), a complex interaction between convection and background wind flow within the predepression Hagupit (2008) was observed by research aircraft at high temporal and spatial resolution.

Predepression Hagupit (2008) developed from an easterly wave propagating along 18°N latitude. Hagupit could be first identified with active convective bursts in satellite imagery on 8 September and with total precipitable water in GFS analysis that was 10–20 mm higher than in the surrounding region around 0000 UTC 9 September (Bell and Montgomery 2010). Then, it was 10 days later at 0000 UTC 19 September 2008 that the predepression was designated as a tropical depression (TD) by the Joint Typhoon Warning Center (JTWC). On average, it takes 3.2 days for a predepression to develop from the convective stage to the TD designation according to Zehr (1992). The delay of predepression Hagupit's development was due in part to its interaction with an upper-level trough during 13–14 September.

In Hagupit's case, the influence from the upper-tropospheric trough was largely unfavorable for TC genesis, but an upper-tropospheric trough can be a favorable ingredient for TC genesis. In the tropical transition paradigm, potential vorticity from the upper-tropospheric trough can be vertically redistributed toward the developing surface vortex through deep convection (Davis and Bosart 2003; Chang et al. 2019). McTaggart-Cowan et al. (2013) showed about 20% of TC genesis in the West Northern Pacific is trough-induced or via tropical transition, and a favorable interaction occurs when the VWS from the upper-tropospheric trough is relatively small and the sea surface temperatures are warm. Similarly, Fischer et al. (2019) found that the upper-tropospheric troughs that are associated with TC rapid intensification (RI) have smaller zonal wavelength and induce smaller VWS over the TC (mostly below $10\,\mathrm{m\,s^{-1}}$) relative to the majority of upper-tropospheric troughs that are associated with non-RI episodes.

The upper-tropospheric trough that Hagupit interacted with induced strong VWS over the predepression. Strong VWS ($>10\,\mathrm{m\,s^{-1}}$) is known to delay or suppress the genesis completely (Tao and Zhang 2014). Several physical mechanisms have been suggested to explain why most TCs weaken in the

---

presence of VWS, including vortex misalignment (Jones 1995), precipitation displacement (Pendergrass and Willoughby 2009; Vigh and Schubert 2009), and ventilation (Tang and Emanuel 2010, 2012). VWS is not always a negative factor for TC genesis though. Recent studies have shown that small to intermediate magnitudes of shear (2.5–$5\,\mathrm{m\,s^{-1}}$) can be actually more favorable for TC formation compared to zero shear (e.g., Nolan and McGauley 2012). We do not fully understand how VWS influences incipient TCs, especially in the context of interaction with midlevel dry air and the parent synoptic-scale precursor (Aiyyer et al. 2014). The presence of moderate VWS (4.5–$11\,\mathrm{m\,s^{-1}}$) in particular increases uncertainty in tropical cyclone (TC) intensity prediction (Rios-Berrios and Torn 2017). The uncertainty arises because many TCs decay in the sheared environment, but a fair amount of TCs withstand the shear impact and even intensify under the same magnitude of VWS.

Hagupit survived the impacts of strong VWS in its early developing phase then ultimately intensified into a TC. Fewer mechanisms have been suggested to explain why some TCs form and intensify in the presence of VWS. In terms of vortex misalignment, Jones (1995) introduced the concept of "vortex precession," which is the advection of one vertical layer of a vortex by the winds of another layer. Through vortex precession, midlevel and low-level vortices can be realigned (e.g., Reasor et al. 2004; Reasor and Montgomery 2015). Molinari et al. (2006) and Nguyen and Molinari (2015) proposed a thermodynamic mechanism that they called "downshear reformation," where the center of the TC reforms underneath the intense convection downshear that is stimulated by the interaction between VWS and the midlevel vortex (Raymond and Jiang 1990). Chen et al. (2018) examined downshear reformation in detail with a case study of typhoon Vicente (2012), and highlighted the role of convective bursts inside the downshear precipitation area in initiating the reformation process through tilting and upward vorticity advection. Rios-Berrios et al. (2018) extended the downshear reformation hypothesis by combining it with the vortex merger paradigm of Van Sang et al. (2008), arguing that the vortex realignment process is not through advective precession but through vortex merger process. The "restructuring" process proposed by Rios-Berrios et al. (2018) starts with the asymmetric precipitation due to VWS then progressively symmetrizes via vortex merger, which reduces vortex misalignment.

All of the aforementioned mechanisms that explain how some TCs withstand VWS require a well-defined midlevel vortex. Although the role of a midlevel vortex is dynamically and thermodynamically essential for TC development (Raymond and Sessions 2014; Bell and Montgomery 2019), for certain period, a predepression may only have a low-level closed circulation (LCC) and not have a midlevel vortex (Reed and Recker 1971). The numerical simulations of tropical cyclogenesis from Wang (2012) showed that the low-level meso-β-scale vortex appears first, then midlevel meso-α-scale vortex follows, and finally the surface meso-α-scale vortex develops. In contrast, some predepression systems that originate from African easterly waves or extratropical disturbances may have a midlevel vortex but no well-developed

LLC (Davis and Bosart 2003; Chang et al. 2019; Pytharoulis and Thorncroft 1999).

In this study, we examine the factors that allow a predepression to survive in a sheared environment with a midlevel vortex that was severely displaced ($>500\,\mathrm{km}$) from the LLC with a case study of Hagupit. We focus on two key factors that enable a predepression to withstand the detrimental effects of environmental shear, namely the wave pouch and localized low-level VWS. First, the Lagrangian closed circulation colloquially called the "wave pouch" can protect the incipient predepression from dry air intrusion (Dunkerton et al. 2009). Keeping moist air in the recirculating wave pouch sustains deep convection due to reduced entrainment and reduced convective downdrafts (Bell and Montgomery 2019). Second, strong mid or low-level shear can actually promote the organization of tropical deep convection (LeMone et al. 1998; Johnson et al. 2005). In this study we consider the combined impact of these two factors, and how VWS and wave-pouch interactions play an important role in cyclogenesis. In particular, we take a novel approach to investigate these interactions across a range of scales from synoptic to meso-γ scale using observational data.

From the two research flight missions over the predepression Hagupit on 14 and 15 September 2008, Bell and Montgomery (2010) provided an unprecedented look at the structure of deep meso-γ-scale convection under the influence of VWS. In this paper, building on Bell and Montgomery (2010), we will investigate what enabled the predepression to survive through the high shear and to eventually undergo cyclogenesis through analysis of these unique aircraft observations, along with large-scale satellite and reanalysis data. The rest of the paper is outlined as follows. Section 2 introduces the datasets from TCS08/T-PARC and the analysis method used in this study. Section 3 describes the results from the multiscale analysis of predepression Hagupit. Section 4 synthesizes the results and provides concluding remarks.

2. Data and methods

For synoptic-scale and meso-α-scale analysis, we used a specialized $0.25°$-resolution Year of Tropical Convection (YOTC) reanalysis (August 2008–July 2009; Rienecker et al. 2008) and the 3-hourly $0.07°$-resolution Grid Satellite (GridSat-B1) data (Knapp 2014). For meso-β- and meso-γ-scale analyses, we used measurements collected during the TCS08/T-PARC field campaigns: the three-dimensional wind field and reflectivity from the high-resolution dual-Doppler radar observation from the Electra Doppler Radar (ELDORA) and soundings from low-altitude (3 km) dropsondes deployed during the aircraft mission around 0000 UTC 14 September 2008. During this flight mission, multiple passes around a convective line between 0030 and 0130 UTC captured the evolution of convective cells in detail.

A variational analysis package called SAMURAI (Bell et al. 2012; Foerster et al. 2014) was utilized in this study to synthesize the observations from radar and dropsondes with a prior estimate of atmospheric state. For the meso-α-scale SAMURAI analysis, ELDORA Doppler velocity and reflectivity

were integrated with dropsonde data at 5-km horizontal and 1-km vertical grid resolution using YOTC thermodynamic and dynamic fields at 0000 UTC 14 September as the prior state estimate. For the meso-β- and meso-γ-scale SAMURAI analyses, we synthesized ELDORA Doppler velocity and reflectivity at 500-m horizontal and vertical grid resolution without a prior estimate or dropsonde data. Gaussian filters with length scales of $4\Delta x$ in the horizontal and $2\Delta z$ in the vertical were used to reduce noise and focus on the scales of interest for each analysis.

To follow the movement of the wave pouch and examine its evolution, we tracked the center of the pouch, defined as the intersection of the critical latitude (where the zonal flow is equal to the wave phase speed) and the wave trough axis (where the meridional velocity is zero), using the YOTC wind field at 850 hPa following Wang et al. (2010). For the phase speed, we used $-5\,\mathrm{m\,s^{-1}}$, the 3-h average phase speed around 0000 UTC 14 September identified from the flight mission, as the default value and tested with a range of phase speed from -2 to $-6\,\mathrm{m\,s^{-1}}$ to accommodate daily variations in easterly wave translation speeds. When the intersection of the critical latitude and the wave trough axis matches with the center of the 850-hPa streamline circulation, we called it the phase speed value at that point in time.

We identify three kinds of vertical wind shear in terms of vertical layers: deep-layer (200–850 hPa), midlevel (500–800 hPa), and low-level (800–1000 hPa) shear. The winds retrieved from ELDORA data have height as the vertical coordinate, thus we use 2–6 km for the midlevel shear and 0–2 km for the low-level shear as equivalent criteria with the pressure coordinate.

To examine the vorticity evolution at the mesoscales, we use the vertical vorticity equation in Cartesian coordinates neglecting the solenoidal term (Holton 2004, p. 101):

$$\frac{D\eta}{Dt} = -\eta\left(\frac{\partial u}{\partial x} + \frac{\partial v}{\partial y}\right) - \left(\frac{\partial w}{\partial x}\frac{\partial v}{\partial z} - \frac{\partial w}{\partial y}\frac{\partial u}{\partial z}\right), \quad (1)$$

where η is absolute vertical vorticity on an f plane, u is zonal velocity, v is meridional velocity, and w is vertical velocity. Equation (1) states that the rate of change of the absolute vorticity following the motion is determined by the stretching and the tilting terms.

3. Results

A wide range of spatial scales was important in predepression Hagupit's genesis. First, we focus on the impacts of the synoptic-scale upper-level trough on the wave pouch at meso-α scale. Then, we will focus on mesoscale processes inside the wave pouch, in terms of localized vertical wind shear, convection, and its associated vorticity generation.

a. Large-scale influences: Trough influences on wave-pouch evolution

A wave pouch became evident on 12 September and was trackable by the intersection of the critical latitude and the wave trough axis. Figure 1 shows vorticity evolution inside the wave pouch from 12 September to 19 September when it was designated as a TD by JTWC. Anomalously high potential vorticity (PV) at 200 hPa was found at the northeast side of the pouch from 13 to 14 September (Figs. 1b,c). Figure 2 shows more evidence of the PV intrusion as an upper-level trough in water vapor satellite imagery with dry northerly air impinging on the predepression (see file ES1 in the online supplemental material for an animation version of this MTSAT-WV imagery).

Streamline analysis of the wave pouch in a Lagrangian framework from 12 to 19 September is shown in Figs. 3 and 4. Prior to the trough interaction, on 12 September, the wave pouch had a weak closed circulation at 850 hPa and an open cyclonic wave at 500 hPa at about 200 km east of LLC center. As a result of strong VWS during 13–14 September, the midlevel circulation became less organized and farther carried away from the LLC center. From 12 to 14 September, the low-level vorticity kept increasing with an approximately closed Lagrangian circulation, but then low-level vorticity decreased, and it became weakest on 15 September. Although the low-level pouch was slightly open at its northwestern corner on 15 September (Fig. 3d), a two-plane mission around 0000 UTC revealed that the LLC was persistent (see file ES2 in the online supplemental material). At the midlevel, a weak circulation was evident on 13 September, but was not evident on 14 or 15 September (Figs. 3f–h). From 16 September, both low-level and midlevel vorticity started to increase again. On 17 September, the pouch obtained a closed LLC again (Fig. 4b), and with northeasterly wind above the easterly wave resulting in northerly vertical wind shear, a midlevel circulation became apparent downshear to the south of the LLC center (Fig. 4f). Figures 4f–h show that vorticity inside the midlevel circulation was aggregating at the midlevel circulation center from 17 to 19 September. Hagupit was designated as a TD on 19 September. At that time, the midlevel circulation was closed and vertically better aligned with the LLC (~100 km apart). From then, the vortex continued intensifying; Hagupit became a category-4 typhoon on 23 September and dissipated after landfall in southern China.

Figure 5 shows the evolution of circulation, relative humidity, and VWS over the wave-pouch area. Figure 5c shows that 200–850-hPa VWS was close to $20\,\mathrm{m\,s^{-1}}$ during 13–14 September averaged over a 6° latitude–longitude square box surrounding the center of pouch. We chose a 6° box size for analysis as a reasonable compromise to capture environmental influences and to represent the thermodynamic and dynamic characteristics inside the wave pouch. The sensitivity to box size is discussed in the next paragraph. In both TC and non-TC environments, VWS most frequently occurs in shallow layers in the upper troposphere (Finocchio et al. 2016); however, the deep-layer VWS is still relevant for the low-level centered wave pouch because the deep convection and stratiform clouds inside the pouch can interact with mid- to upper-tropospheric shear. Under the strong VWS, mid- to upper-level circulation over the wave-pouch area decreased significantly, and on 14 September it became anticyclonic (Fig. 5a). Low-level circulation, in contrast, kept increasing until 14 September and persisted during the time of strong VWS. Both midlevel and low-level circulation reached a minimum on 15 September and then started to increase again
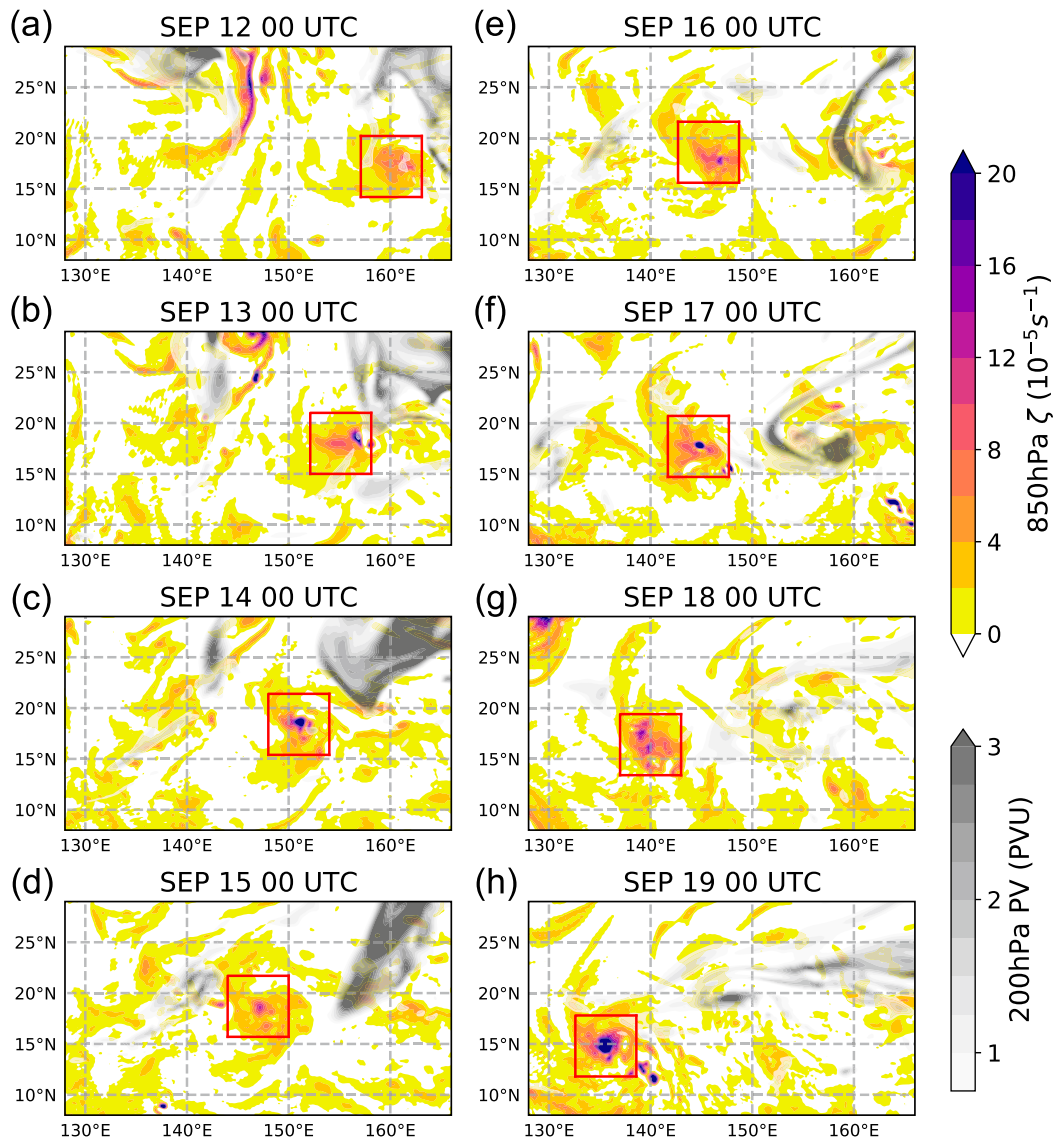
FIG. 1. Vorticity at 850 hPa around predepression Hagupit from 0000 UTC 12 Sep to 0000 UTC 19 Sep. Red-outlined boxes are 6° × 6° centered on Hagupit's wave pouch at each time. The potential vorticity field at 200 hPa is contoured in grayscale.

on 16 September. There was some dry air intrusion on 14–15 September resulting in a decrease in relative humidity around 700–850 hPa (Fig. 5b).

Figure 6 shows the average circulation, low-level/midlevel vorticity, VWS, column water vapor (CWV), and infrared brightness temperature as a function of time for different box sizes following the pouch center. The wave pouch had vorticity and moisture concentrated near the pouch center; the average values decrease when they are averaged over bigger square box (Figs. 6c–e). On the other hand, circulation (Fig. 6a), which is equal to the integral of vorticity inside the box, increases as the box size increases up to 8°, then decreases due to contributions of negative vorticity outside of the pouch (see Figs. 3 and 4). Vertical wind shear magnitude

(Fig. 6b) is not as sensitive to the box size because it is induced by a synoptic-scale trough.

It is interesting that CWV kept increasing without any hiatus despite the strong VWS during 13–14 September (see Figs. 6b,d). Geostationary Infrared brightness temperature (BT) analysis revealed convective bursts having BT colder than −60°C consistently inside the wave pouch (Fig. 6f, and Fig. S3). The cold cloud fraction over the wave-pouch area (green line in Fig. 6f) shows persistent diurnal pulses of convective bursts for 13–15 September. We hypothesize that this consistent convection was still moistening the air column inside the wave pouch on 13 and 14 September. CWV decreased on 17 September under weaker deep-layer (200–850 hPa) VWS compared to 13–14 September, but stronger
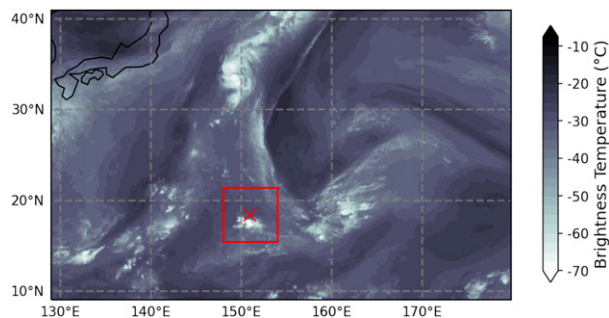
FIG. 2. MTSAT infrared water vapor channel (near 6.7 μm) brightness temperature showing predepression Hagupit and upper-level trough to the northeast at 2335 UTC 13 Sep. The red-outlined box is 6° × 6° around the pouch center. An animated version this figure is available (see file ES1 in the online supplemental material).

midlevel (500–850 hPa) VWS (see Fig. 5c). Midlevel VWS could be more detrimental to column moistening than deep-layer VWS especially for weaker TCs (Finocchio et al. 2016). However, Fig. 6c shows that CWV near the pouch center did not decrease significantly and remained over 60 kg m^{-2} until genesis. It is noteworthy that Hagupit was designated as a TC only after the pouch had deepened and acquired a well-defined midlevel vortex. Comparing Figs. 6e and 6f, there is a correlation between the rapid increase in midlevel vorticity and cloud top height, indicated by the median BT, over the wave-pouch area around 0000 UTC 18 September.

Overall, the reanalysis suggests that the wave pouch was able to protect the low-level circulation and moisture during the upper-level PV intrusion on 13–14 September, although the pouch became quite shallow as the midlevel vortex became misaligned or completely dissipated. In the following subsection, we will examine the dynamics and thermodynamics on the mesoscale inside the wave pouch during this interaction with the upper-level trough on 14 September.

b. Upscale vortex merger process: Vortical convection in a sheared predepression

A research flight was conducted into predepression Hagupit around 0000 UTC 14 September. In the following section, we investigate the complex local impacts of the VWS on organization and development of convection using high-resolution dual-Doppler radar data (500 m grid spacing) with a short time interval (7 min) and vertical thermodynamic profiles from dropsondes. Furthermore, we assess the upscale impacts of the meso-γ- and meso-β-scale convective structures on the tropical cyclogenesis of predepression Hagupit.

MESO-β AND MESO-γ SCALES: LOCALIZED SHEAR AND CONVECTION

The flight track and the locations of 14 dropsondes deployed during the mission are shown in Fig. 7, overlaid over a visible satellite image of Hagupit. The research aircraft flew around 700-hPa pressure level, and the wind barbs indicate winds at

1000 hPa measured by the dropsondes. The wind barbs show a weak cyclonic circulation near the surface with a center that corresponds well with the pouch center, indicated by the red star (18.4°N, 151°E), calculated from the 850-hPa YOTC reanalysis velocity field. Convection was located to the west and south of the LLC center.

In the red-outlined box in Fig. 7, the convection is organized linearly like a squall line from north to south. Figure 8 zooms in on this convective region and shows vertical vorticity at 2-km altitude calculated from the dual-Doppler analysis overlaid on the radar reflectivity. Two subregions along the convective line denoted North (N) and South (S) box are highlighted in Fig. 8a. Figures 8b,c and 8d,e show the snapshots of N box and S box in seven minute intervals, respectively. The average 2-km reflectivity of the N box is larger than that of the S box. The reflectivity did not change much in 7 min, but the vorticity evolved noticeably within the same period. There are newly generated vorticity maxima and also several dissipating vortical structures.

Here we focus on the vortical structure of one convective cell in each box (N cell and S cell in Fig. 8) that are representative of multiple convective cells in each box. Vorticity budget analysis was conducted for the two cells using Eq. (1). The left columns of Figs. 9 and 10 are snapshots of the cells at 0033 and 0125 UTC, respectively. The right columns are seven minutes later (0040 and 0132 UTC). In the first two rows of Figs. 9 and 10, the stretching and tilting vorticity generation terms are contoured on reflectivity at 2-km altitude. It was not possible to close the vorticity budget due to nonnegligible horizontal advection over the 7-min time interval and missing wind data in clear air. The residual was of the same order of the magnitude (10^{-6} s^{-2}) as all of the other budget terms.

Starting from Fig. 9a, the N cell has a local maximum in stretching larger than 6×10^{-6} s^{-2} collocated with a reflectivity maximum above 50 dBZ. The large stretching term results from low-level convergence coincident with a vertical vorticity maximum shown in Fig. 9c. Then, seven minutes later, the magnitude of the stretching term significantly decreased (Fig. 9f) as the low-level convergence decreased rapidly while the vorticity persisted (Fig. 9h). While the low-level convergence decreased, the updraft at 7-km altitude increased from 12 to 15 m s^{-1} (Figs. 9e,j). Overall, the N cell appears to be a mature cell starting to decay. Although the convection was still active as evidenced by the growing updraft, by 0040 UTC it had lost the low-level supporting convergence.

The S cell had several pronounced differences from the N cell in its vorticity evolution (Fig. 10). The S cell was captured during its rapidly developing stage. The maximum reflectivity of the S cell is about 15 dBZ lower than that of the N cell (N cell's maximum above 50 dBZ and S cell's maximum between 35 and 40 dBZ). During the 7-min interval displayed in Fig. 10, S cell's 2-km vorticity and 7-km updraft magnitude tripled. The stretching term cannot explain this vigorous vorticity increase. Prior to the vorticity increase at 0125 UTC the stretching term was not apparent at 2 km (Fig. 10a), and there was no significant low-level convergence either (Fig. 10c). A positive tilting term is collocated with a weak low-level vorticity center near
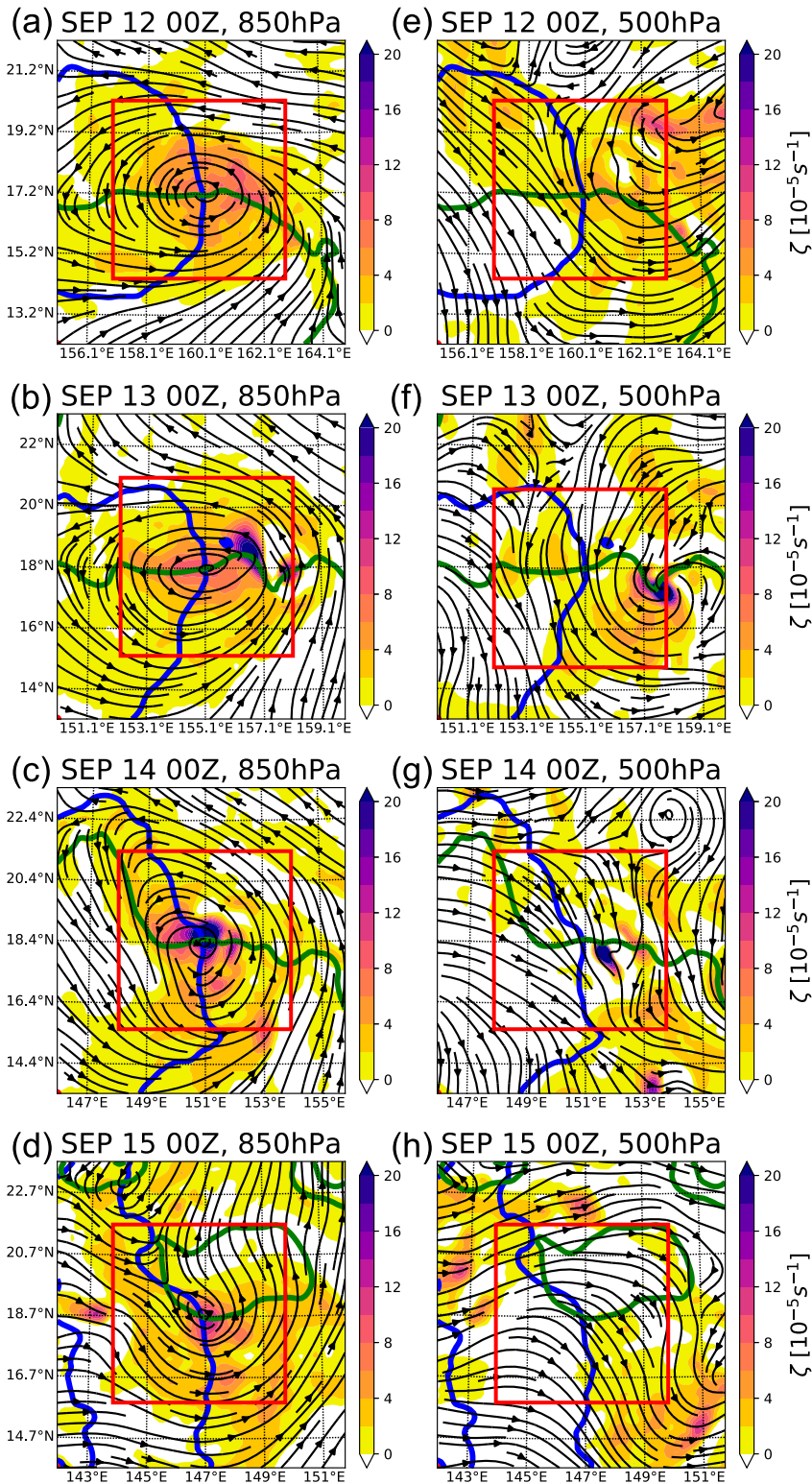
FIG. 3. Streamlines (black contours) and vertical relative vorticity (color shading) from 12 to 15 Sep at (a)–(d) 850 and (e)–(h) 500 hPa around Hagupit's wave pouch. Green lines indicate the critical latitude (where the zonal flow is equal to the wave phase speed), and blue lines indicate the wave trough axis (where the meridional velocity is zero) at 850 hPa. The center of the wave pouch is defined as the intersection of the green and blue lines. The red-outlined box is 6° × 6° around the pouch center.
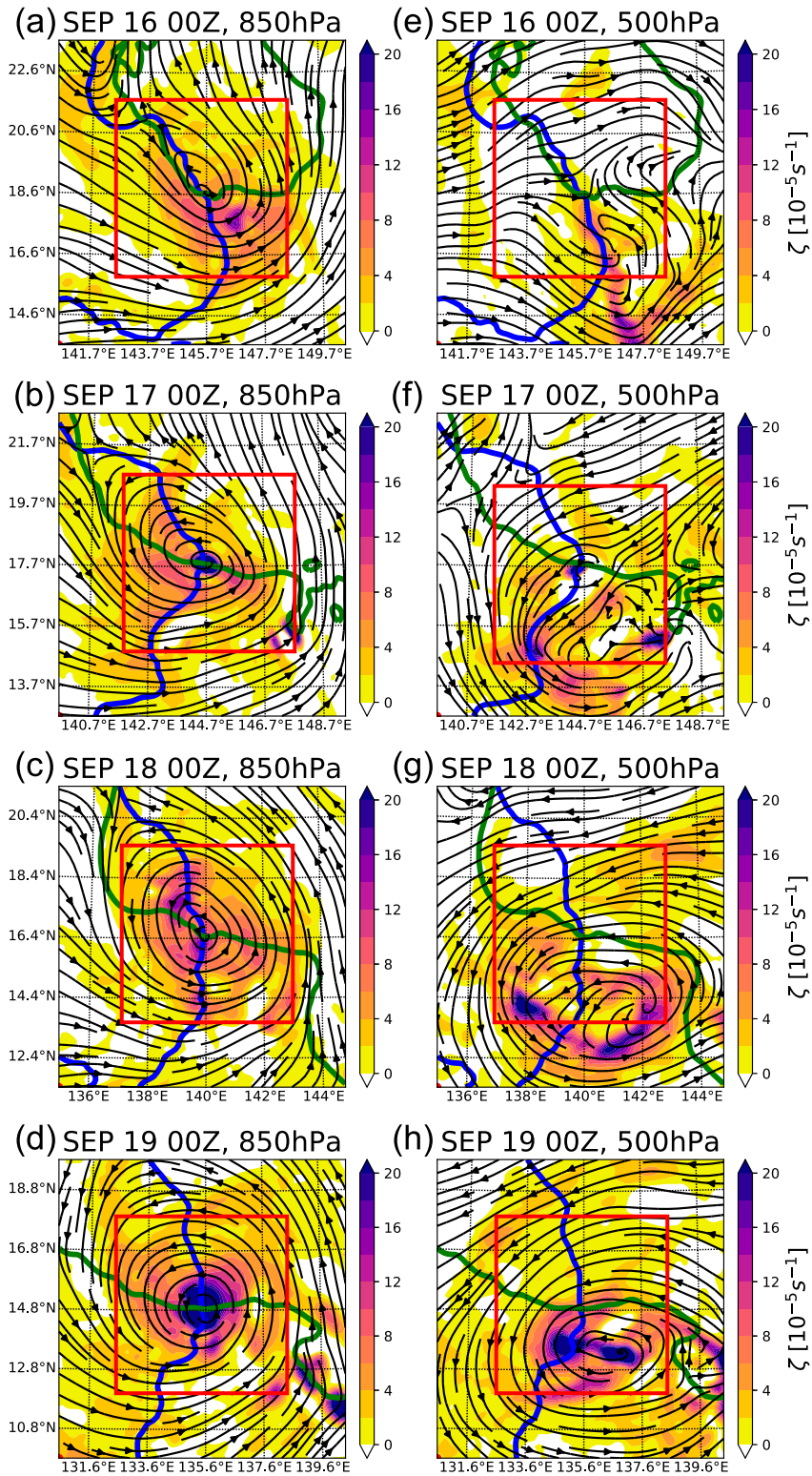
FIG. 4. As in Fig. 3, but from 16 to 19 Sep.
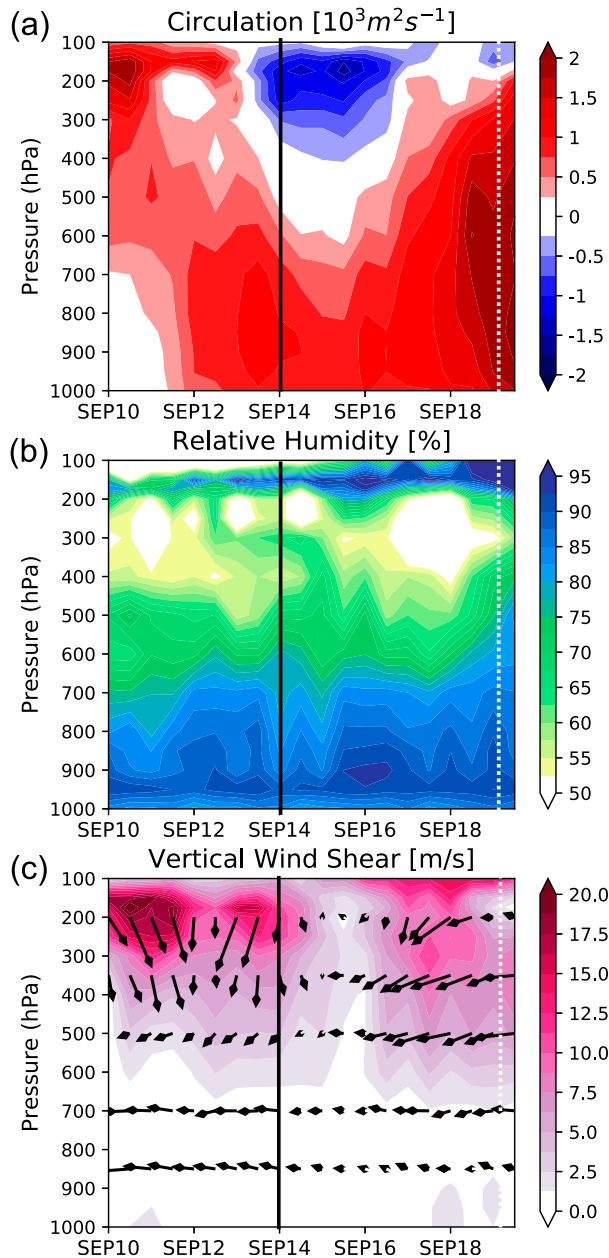
FIG. 5. Time series of vertical structure inside Hagupit's wave pouch (12 hourly averaged over 6° × 6° box): (a) circulation, (b) relative humidity, and (c) vertical wind shear (VWS) magnitude (color shades) and wind direction (vectors) from 0000 UTC 10 Sep to 1200 UTC 19 Sep. VWS was calculated between each pressure level minus wind at 850 hPa. The vertical black line indicates the aircraft mission (0000 UTC 14 Sep), and the white dotted vertical line marks when Hagupit was designated as a tropical depression by the Joint Typhoon Warning Center (0000 UTC 19 Sep).

where the convection erupts. Figure 10d shows a weak updraft at 2 km was tilting the northwestward horizontal vorticity vector, which partially contributed to the increase in positive vertical vorticity. By 0133 UTC, the stretching term became the dominant source of vorticity generation as low-level

westerly winds increased on the west side of the domain (Fig. 10f), resulting in a large value of low-level convergence collocated with the vorticity maxima (Fig. 10h). The difference of tilting-dominant and stretching-dominant vorticity generation mechanism between S cell and N cell can be explained by two factors: 1) local low-level wind shear and 2) the stage of the convective life cycle. These factors are further explored using the aircraft observations in the following paragraphs.

Figures 11 and 12 compare the vertical wind profile and vertical cross sections of N cell and S cell. Vertical wind profiles inside N box and S box, obtained by the four dropsondes and dual-Doppler radar data, are plotted on the hodographs in Figs. 11a,b and 12a,b. Dropsonde winds are plotted with cooler colors and radar-retrieved winds are plotted with warmer colors. Dropsonde profiles are available from the surface to the aircraft flight level of 700 hPa (3 km). Winds from dual-Doppler radar are averaged over the 40 km × 40 km N box and S box to represent the meso-β-scale vertical wind profile. The winds from dropsondes and radar are generally in good agreement, although radar low-level winds represent a larger spatial scale than the dropsondes due to coarser vertical resolution and meso-β-scale averaging.

For the N box, the wind was predominantly from the east or east-northeast around 7.5 m s^{-1} from the surface to 5 km (Figs. 11a,b). Low-level (from the surface to 3 km) wind shear produces horizontal vorticity that is then available for tilting into the vertical. The minimal low-level wind shear in the N box explains why the N cell did not have appreciable low-level tilting at this time. In mid- to upper levels, the wind direction and speed changes to strong northerlies due to the upper-level trough, producing large shear aloft. A vertical cross section in the N cell (Figs. 11c,d) suggests that the cell was in a mature stage and near the end of the convective life cycle. Between 0033 and 0040 UTC, the reflectivity and the vorticity in the low levels decreased. In the upper levels, the echo top of N cell had grown from 12 to 16 km and a very intense vorticity dipole formed above 10 km over the 7 min. The dipole is likely due to tilting of shear-generated horizontal vorticity associated with the upper-level trough.

One noticeable difference between N box and S box is that the low-level shear in the S box is stronger, exceeding 8 m s^{-1} (Fig. 12). As a result, the S box had more horizontal vorticity, which could be tilted into vertical (Fig. 10i). In mid- to upper levels, the wind patterns in both the N box and the S box are similar and dominated by the synoptic-scale easterly wave and upper-level trough. The S box has weaker upper-level northerlies compared to the N box, as it is relatively farther from the trough. Near-surface winds are largely determined by the position relative to the LLC, which persisted despite the strong deep-layer VWS. The N box was located to the northwest from the LLC center, while the S box was to the west (Fig. 7); the near-surface winds shift from east-northeast in the N box to more northerly in the S box, resulting in different low-level VWS across the 80-km distance between the two boxes. The northerly midlevel shear (2–6 km) in N box is parallel to the N–S linear organization in Figs. 8b and 8c. The east-southeasterly strong low-level shear in S box is near parallel to the NW–SE linear squall-line-like convection shown in
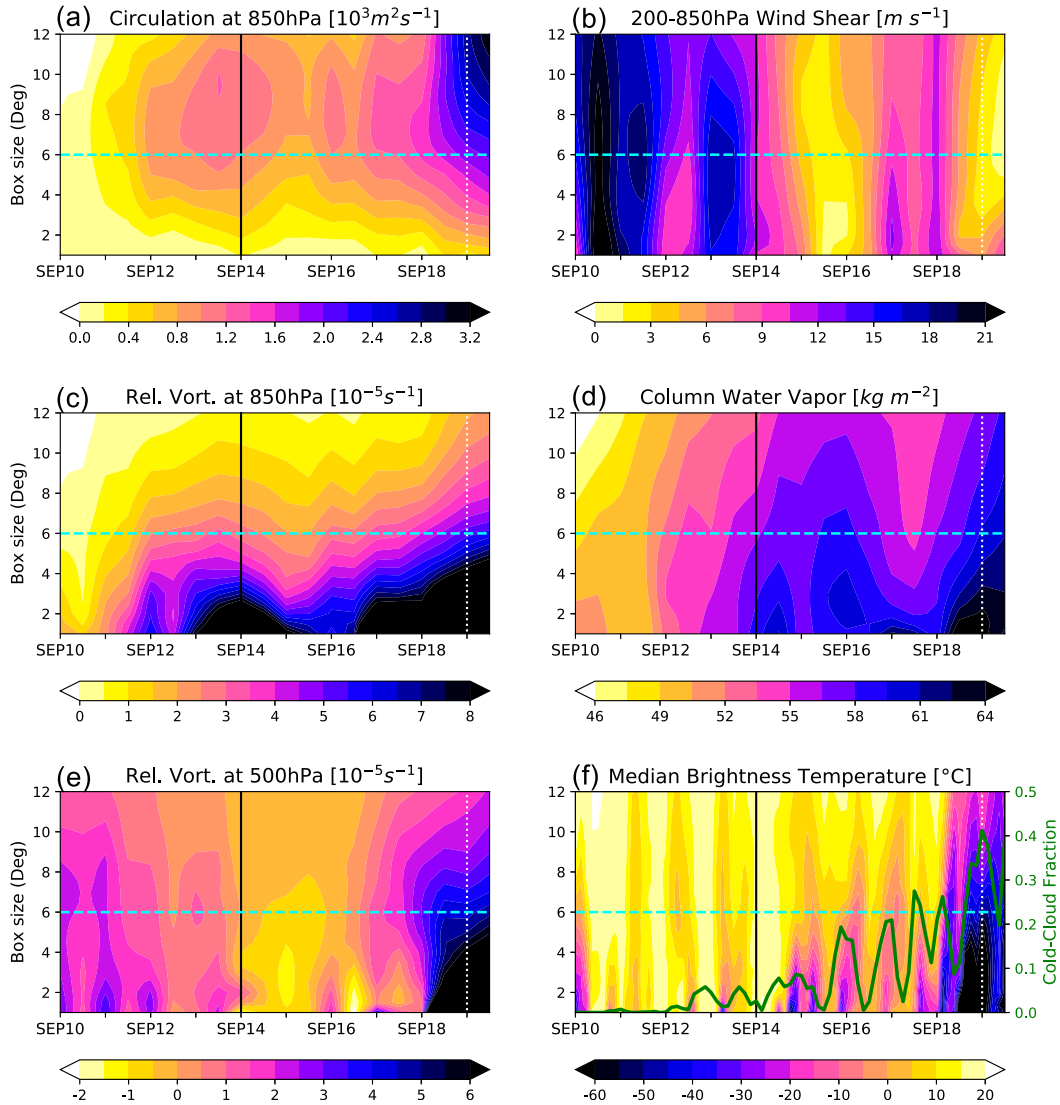
FIG. 6. Thermodynamic and dynamic quantities averaged over the box centered on the wave-pouch center as a function of time (from 10 to 19 Sep) and box length: (a) circulation at 850 hPa, (b) 200–850-hPa vertical wind shear, (c) relative vorticity at 850 hPa, (d) column water vapor, (e) relative vorticity at 500 hPa, and (f) median brightness temperature (BT) from the infrared window channel (near 11 μm). The green line in (f) shows the fractional coverage of cloud tops of −60°C or colder within the 6° × 6° square box around the pouch center. An animation of MTSAT infrared BT overlaid on a latitude–longitude map is available (file ES3 in the online supplemental material). Cyan dashed lines indicate the box size that is used in our meso-α-scale analysis. The black solid and white dotted lines denote the aircraft mission and genesis as in Fig. 5.

Figs. 8d and 8e. This shear and convective structure relationship is consistent with the findings of LeMone et al. (1998) and Johnson et al. (2005), which will be detailed in the Discussion section.

Skew T–log$p$ diagrams show lower convective inhibition (CIN) and higher convective available potential energy (CAPE) in soundings in the S box (Figs. 12a,b) than in soundings in the N box (Figs. 11a,b). The soundings suggest that the S box had a slightly more favorable thermodynamic environment for new convective cells to emerge. In Figs. 12c and 12d, the S cell has an echo top below 8 km with increasing reflectivity and vertical

vorticity from the low- to midlevels between 0125 and 0132 UTC. The S cell could be classified as a cumulus congestus in the early stage of the convective life cycle based on the echo top height and its convective characteristic (Johnson et al. 1999).

Using the N and S cells as representative of the convective and vortical evolution from cumulus congestus to mature deep convection, the analysis suggests that vorticity generation starts from tilting of the ambient horizontal vorticity into the vertical from the initial convective updraft. Enhanced low-level convergence follows as the buoyant plume rises and
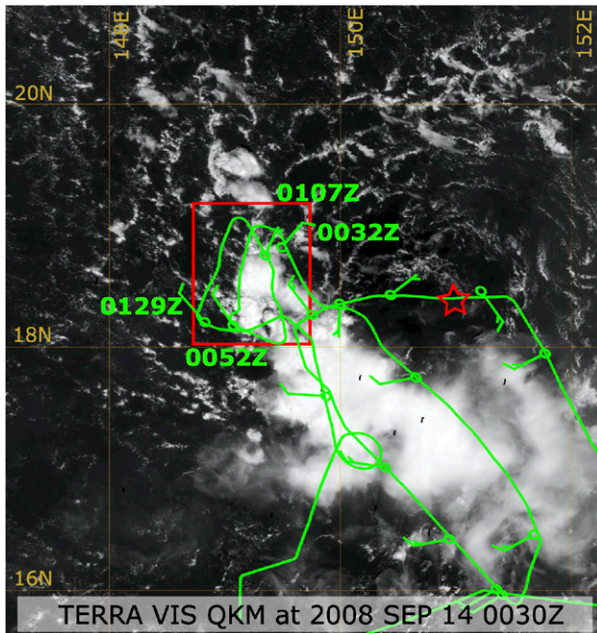
FIG. 7. Visible satellite image with flight track around 700-hPa level (green line) and wind barbs denoting 1000-hPa winds measured by dropsondes deployed from the flight mission. The center of the wave pouch (18.4°N, 151°E) is indicated by a red-outlined star. The red-outlined box denotes the radar analysis domain in Fig. 8a, below.

stretches the vertical vorticity. As the convective cell matures, the buoyancy is consumed and low-level convergence and vorticity decrease. The results suggest that the low-level vertical vorticity generated through the convective life cycle outlives the convection consistent with Wissmeier and Smith (2011) and Kilroy et al. (2014). The role of low-level VWS in helping the convective organization inside the wave pouch and providing ingredients for vorticity amplification via tilting, will be discussed further in the concluding section.

c. Meso-α scale: Vorticity accumulation inside the wave pouch

Here we quantify the upscale cascade from meso-γ-scale vorticity generation to meso-α-scale system development. Figure 13 shows reflectivity and wave-relative meso-α-scale winds from the flight mission on 14 September (see Fig. 7 for flight track). Streamlines at 10-km altitude (blue) show northwesterly wind over the whole domain associated with the upper-level trough to the northeast of Hagupit. At 1-km altitude, a weak but closed cyclonic circulation is apparent in the wave-relative frame. The convection is not symmetric around the LLC center. The strong convective line, closely examined on meso-β and meso-γ scales in the previous section, was located to the west of the circulation center. A broad region of stratiform precipitation was located to the south of the LLC center, cyclonically downstream of the convective area. This pattern of the convective initiation at downshear right quadrant and a wider region of stratiform in downshear left is in agreement with the previous studies that have examined the

shear-relative convective characteristics of TCs (Corbosiero and Molinari 2002; DeHart et al. 2014), but it is an open question as to whether this pattern is due to the same mechanism suggested by the previous studies since the predepression Hagupit did not have a well-defined midlevel vortex above at this point.

The circulation associated with the convective (orange) and stratiform (green) regions is calculated along the perimeter of each box in Fig. 13b. To examine the impacts of convective activity on the circulation, the stretching tendency in each box is calculated as $-\oint \eta \mathbf{V} \cdot \hat{n} \, dl$ [see Eq. (3) of Davis and Galarneau (2009) for the detailed circulation tendency equation]. Although the role of tilting in vorticity generation was highlighted above from the meso-γ-scale analysis, the tilting contribution on the meso-α-scale was near-zero (not shown).[1] On 14 September, the YOTC analysis shows that circulation of predepression Hagupit was decreasing throughout the whole vertical column (Fig. 5), yet the mesoscale radar analysis indicates that vertical vorticity was being actively generated through stretching in the convective area. The depth of the cyclonic circulation was generally below 4–6 km (Fig. 13b), and the convective region had positive stretching from the surface up to 6 km (Fig. 13c). While the convective region shows positive circulation maximized near the surface, the stratiform region shows two peaks in the vertical profile of circulation: one near the surface and another in the midlevel around 5 km (Fig. 13b). As shown in Fig. 13c, stratiform precipitation has midlevel convergence and low-level divergence and thus positive stretching at the midlevels and negative at the low levels. At the level of maximum convergence in the stratiform region of an MCS, a midlevel mesoscale convective vortex (MCV) can form (e.g., Houze 2004).

Once created, the vorticity generated in the convective and stratiform areas outlives the convection (Fang and Zhang 2011; Wissmeier and Smith 2011; Davis 2015). Thus, vorticity can be accumulated inside the closed circulation of the pouch, and aggregated through a vortex merger process (Van Sang et al. 2008). The results presented here support the conclusions of previous studies that argued that deep convection plays a primary role in genesis by generating vorticity through stretching (Ooyama 1969; Zehr 1992; Raymond et al. 1998; Bell and Montgomery 2019). The results are consistent also with the hypothesis of Bell and Montgomery (2019) that stratiform precipitation that forms from the waning convection plays an important supporting role by strengthening the midlevel circulation.

4. Discussion and conclusions

Figure 14 summarizes the key results from this study and the multiscale interactions of Hagupit's cyclogenesis in a sheared environment. This telescoping schematic depicts the important

---

[1] Lifting of a horizontal vortex line produces a dipole of vorticity, such that tilting only affects the circulation if the dipole straddles the boundary. To test the sensitivity to the boundary, we took the ensemble mean of nine different boxes around the convective and stratiform regions (dotted boxes in Fig. 13a). Taking the ensemble-mean of the tilting term for the nine boxes with 10-km-shifted locations resulted in near-zero net impacts of tilting.
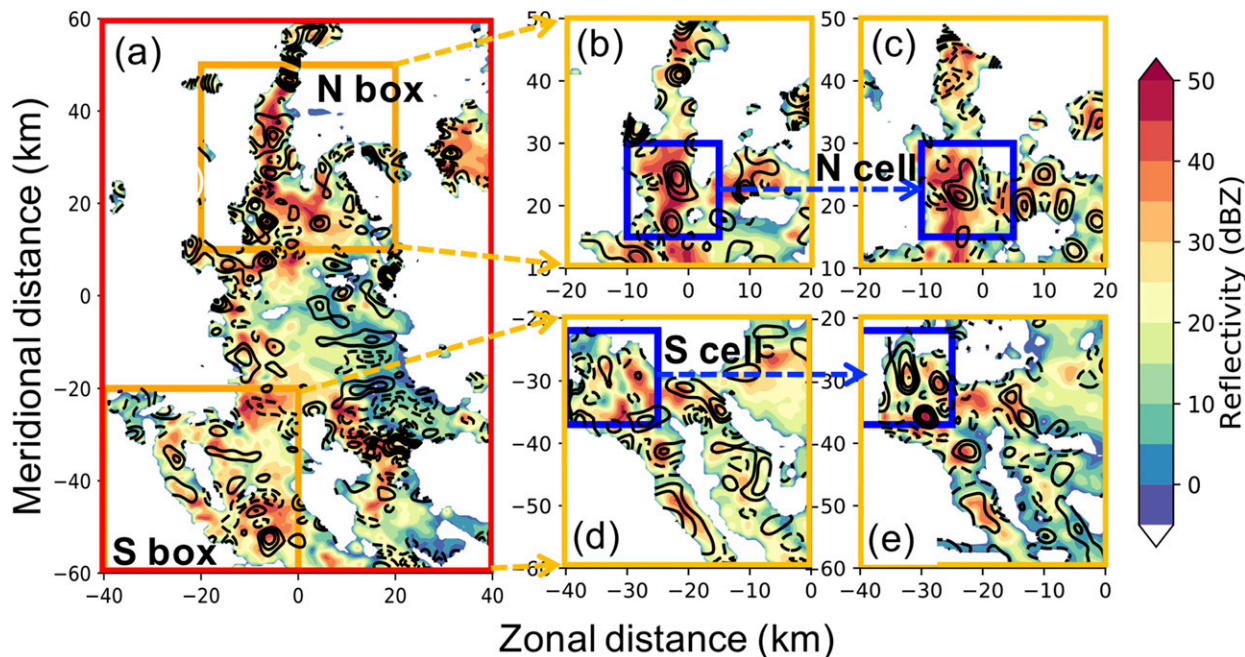
FIG. 8. Radar reflectivity (shading; dBZ) and vertical vorticity (contours; $1 \times 10^{-3}\,\mathrm{s}^{-1}$ with zero omitted and negatives denoted by dashed lines) at 2 km in the zoomed-in domain of the convective area inside the wave pouch of predepression Hagupit around 0000 UTC 14 Sep, showing (a) radar observation composited for 0058–0114 UTC inside the 120 km × 80 km domain (red-outlined box in Fig. 7). The yellow-outlined boxes in (a) are zoomed in for more detail: N box in the time periods of (b) 0030–0037 UTC and (c) 0037–0043 UTC and S box in the time periods of (d) 0121–0128 UTC and (e) 0128–0135 UTC.

factors at each spatial scale inside the circles. The most important factors at synoptic scale (Fig. 14a) include the upper-level trough and easterly wave carrying the marsupial wave pouch. The recirculating wave pouch is at meso-α scale (Fig. 14b), and it is the focal point where the downscale influences from synoptic scale and the upscale cascade from meso-β and -γ scales meet. At meso-β scale (Fig. 14c), the local VWS profile and its impact on squall-like convective organization is illustrated. Finally, at meso-γ scale (Fig. 14d), there are convective cells producing vorticity through stretching and tilting through interaction of the updraft with the local shearing flow throughout the convective life cycle. Below, we will discuss each circle in more detail incorporating the relevant results.

Tropical cyclogenesis of predepression Hagupit was delayed while it interacted with upper-level trough, experiencing strong VWS. For the downscale influences from the synoptic to meso-α scale, our analysis showed that predepression Hagupit was significantly affected by the strong northerly vertical wind shear. The midlevel vortex of the predepression was shifted to southeast (Fig. 14b yellow cross), and became misaligned with the low-level vortex by more than 5° (Figs. 3 and 4). In addition to the vortex misalignment, convective precipitation was shifted to the southwest of the LLC center (Figs. 7, 13a, and 14b).

However, Hagupit survived through the hostile, strongly sheared environment, and eventually developed into a tropical cyclone after it escaped from the influence of upper-level trough. Despite the shear and misalignment, the low-level circulation inside the wave pouch persisted through 13–14 September. Then, during 16–17 September the wave pouch deepened and

developed a midlevel vortex, which ultimately led to designation as a tropical depression on 19 September (Figs. 5a and 6e). It is hypothesized that the upscale cascade from the persistent deep convection (Fig. 6f) and its vorticity amplification through vortex tube stretching (Figs. 13 and 14d) was a key process that enabled the pouch to persist even under strong VWS. The localized vertical vorticity generated from deep convective cells is aggregated through a vortex merger process in the closed Lagrangian circulation inside the marsupial pouch (Fig. 14b).

In the meso-β-scale circle (Fig. 14c), we illustrate the localized shear profile and how that impacts the organization of the convective cells and vortical characteristics of the MCSs inside the wave pouch. The shear profile depended on the distance from the upper-level trough and relative location from the LLC center (Fig. 12). In comparing the meso-β-scale N box and S box, it is seen that the influence of the trough is reduced to the south while the magnitude of low-level shear is increased across the 100-km distance. The midlevel shear (500–800 hPa) was generated by the difference between the easterly wind and the upper-level trough. The low-level shear (800–1000 hPa) was generated by the difference between the cyclonic circulation near the surface and easterly wind at midlevels associated with the easterly wave.

The linear organization of convection in the N box and S box can be explained by the low-level and midlevel shear configuration in each box. LeMone et al. (1998) proposed a conceptual framework for the relationship between the shear profile and the mesoscale convective structure in the tropics based on the Tropical Ocean Global Atmosphere Coupled Ocean–Atmosphere Response Experiment (TOGA COARE), and Johnson et al. (2005) added
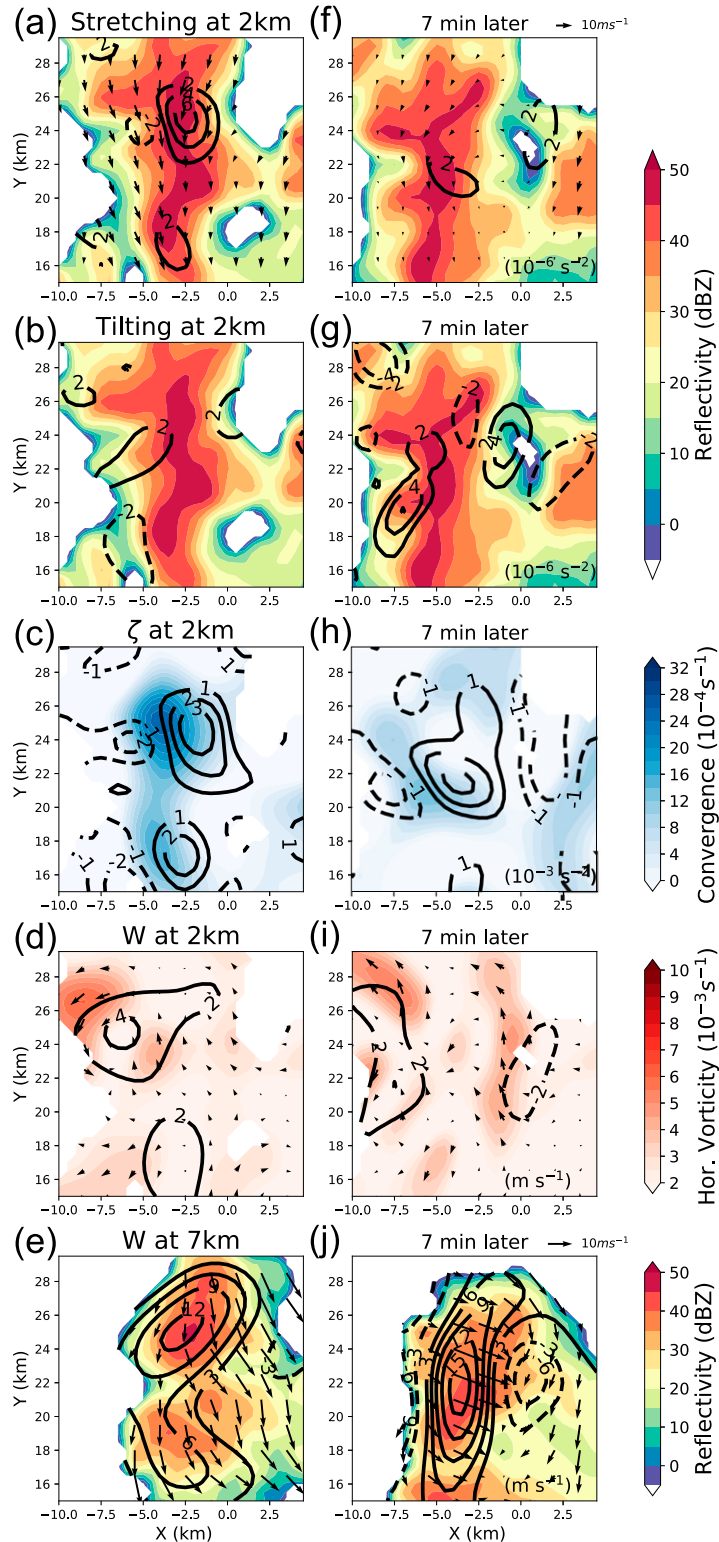
FIG. 9. Meso-γ-scale evolution of N cell from the (left) 0030–0037 UTC flight to (right) 0037–0043 UTC flight: (a),(f) radar reflectivity (shading), stretching (contours), and horizontal wind velocity (vectors) at 2 km with the 7-min time interval; (b),(g) as in (a),(f) but tilting at 2 km as contours, (c);(h) convergence (shading) and vertical vorticity (contours) at 2 km; (d),(i) horizontal vorticity magnitude and direction (shading and vectors, respectively) and vertical velocity (contours) at 2 km; and (e),(j) radar reflectivity (shading), vertical velocity (contours), and horizontal velocity (vectors) at 7 km. For all contours, zeros are omitted and negative values are denoted with dashed lines.
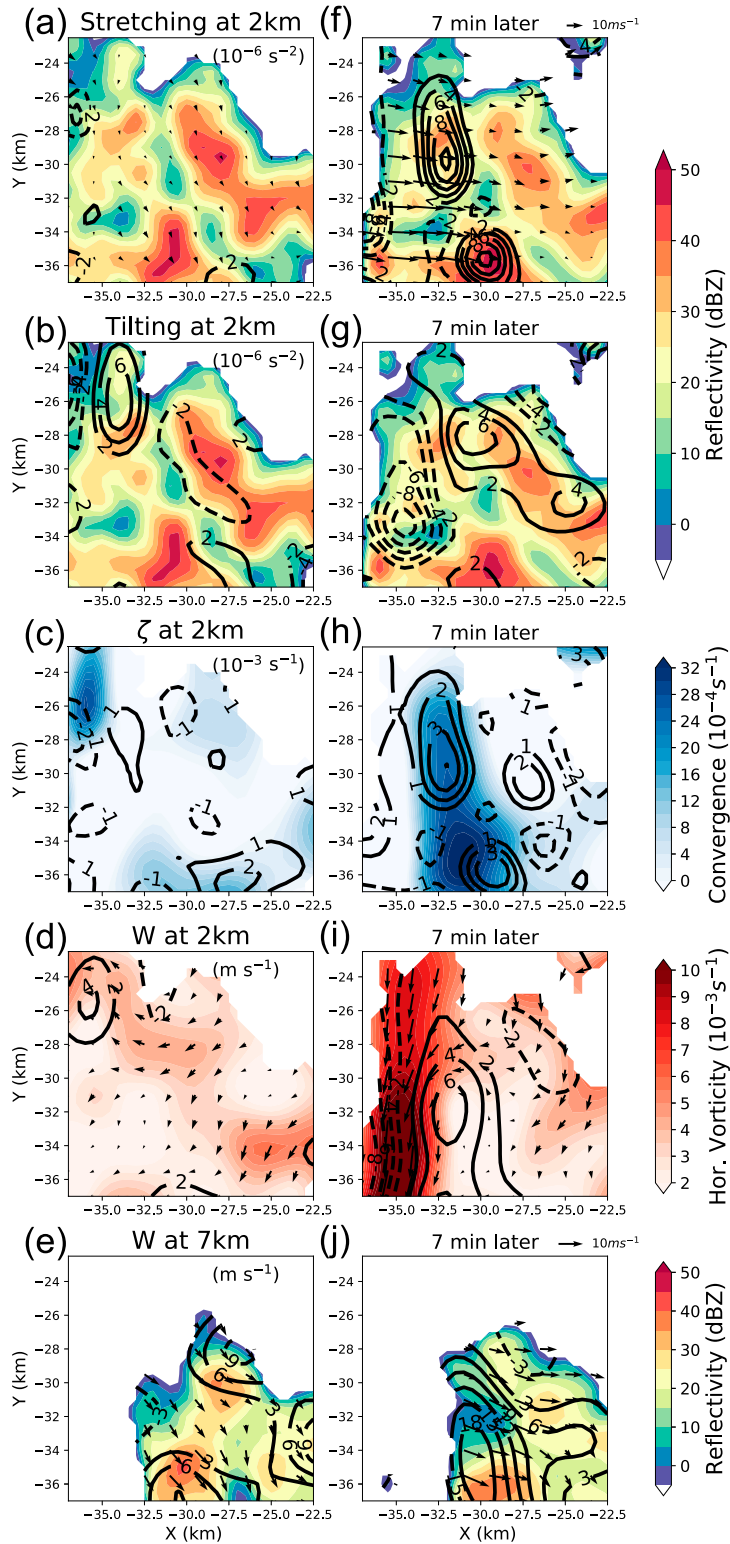
FIG. 10. As in Fig. 9, but for the S cell from the (a)–(e) 0121–0128 UTC flight to (f)–(j) 0128–0135 UTC flight.
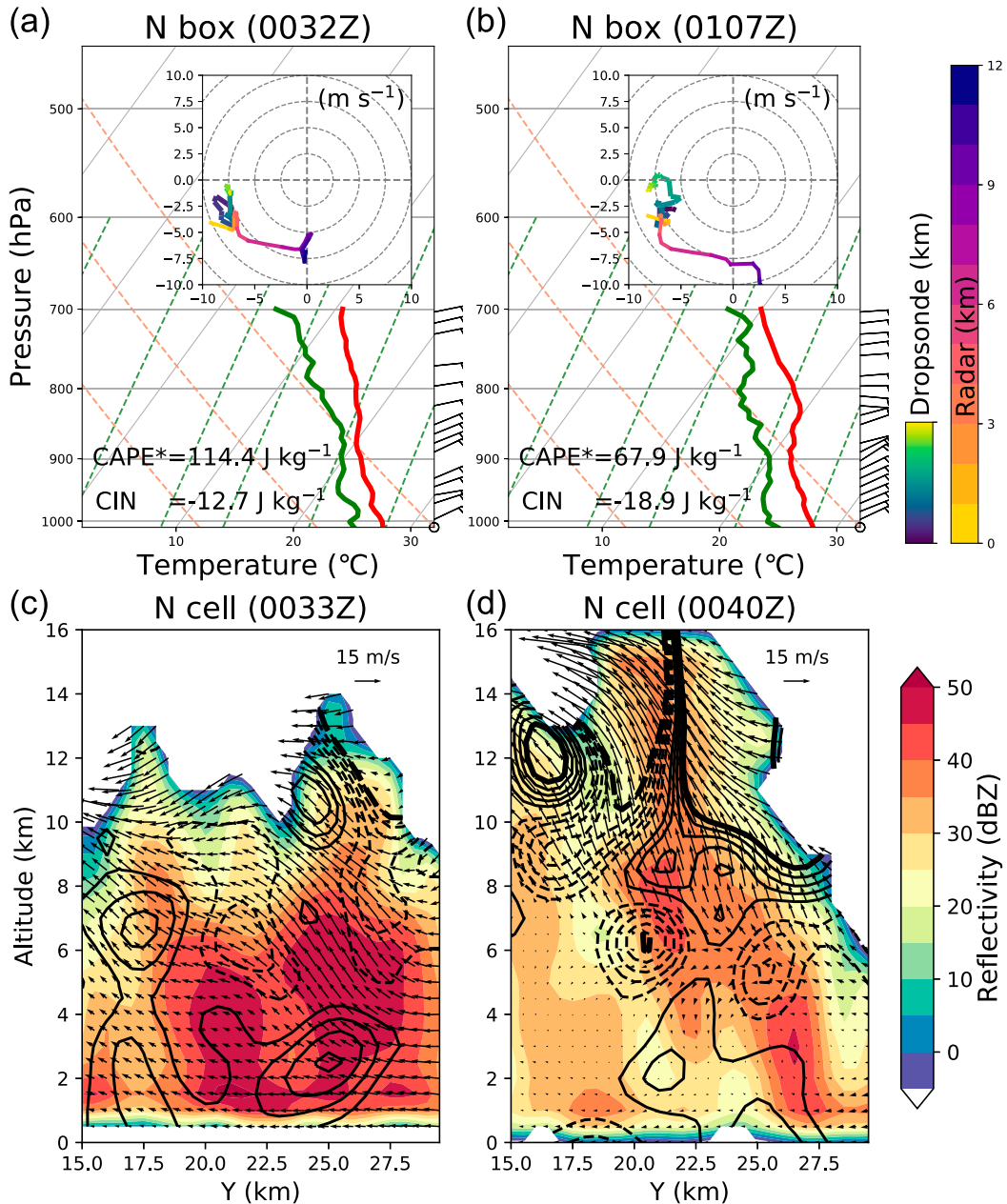
FIG. 11. Thermodynamic and convective evolution in the N box (see Fig. 8): Skew T–log$p$ diagram from drop-sondes deployed at (a) 0032 and (b) 0107 UTC 14 Sep at the locations indicated in Fig. 7. The red line is air temperature, the green line is dewpoint temperature, red dashed lines are dry adiabats, and green dashed lines are mixing ratio. Convective inhibition (CIN) and convective available potential energy (CAPE) are calculated on the basis of a parcel at the surface for 1000–700 hPa. Hodographs inside the skew T–log$p$ diagrams are from dropsonde observation and wind retrieved from dual-Doppler radar at 0024–0037 for (a) and 0058–0114 UTC for (b), averaged over the N box. Also shown are vertical cross sections of convective cell inside the N box (N cell) at (c) 0033 and (b) 0040 UTC. Radar reflectivity is shaded, and vertical vorticity is shown with $2 \times 10^{-3}\,\mathrm{s}^{-1}$ contours (zero is omitted, negatives are denoted by dashed lines, and absolute magnitudes $10 \times 10^{-3}\,\mathrm{s}^{-1}$ are shown as thicker lines, with values bigger than that omitted). Wave-relative winds are shown with vectors. The N-cell cross section is taken along $X = -2\,\mathrm{km}$ in Fig. 8b.
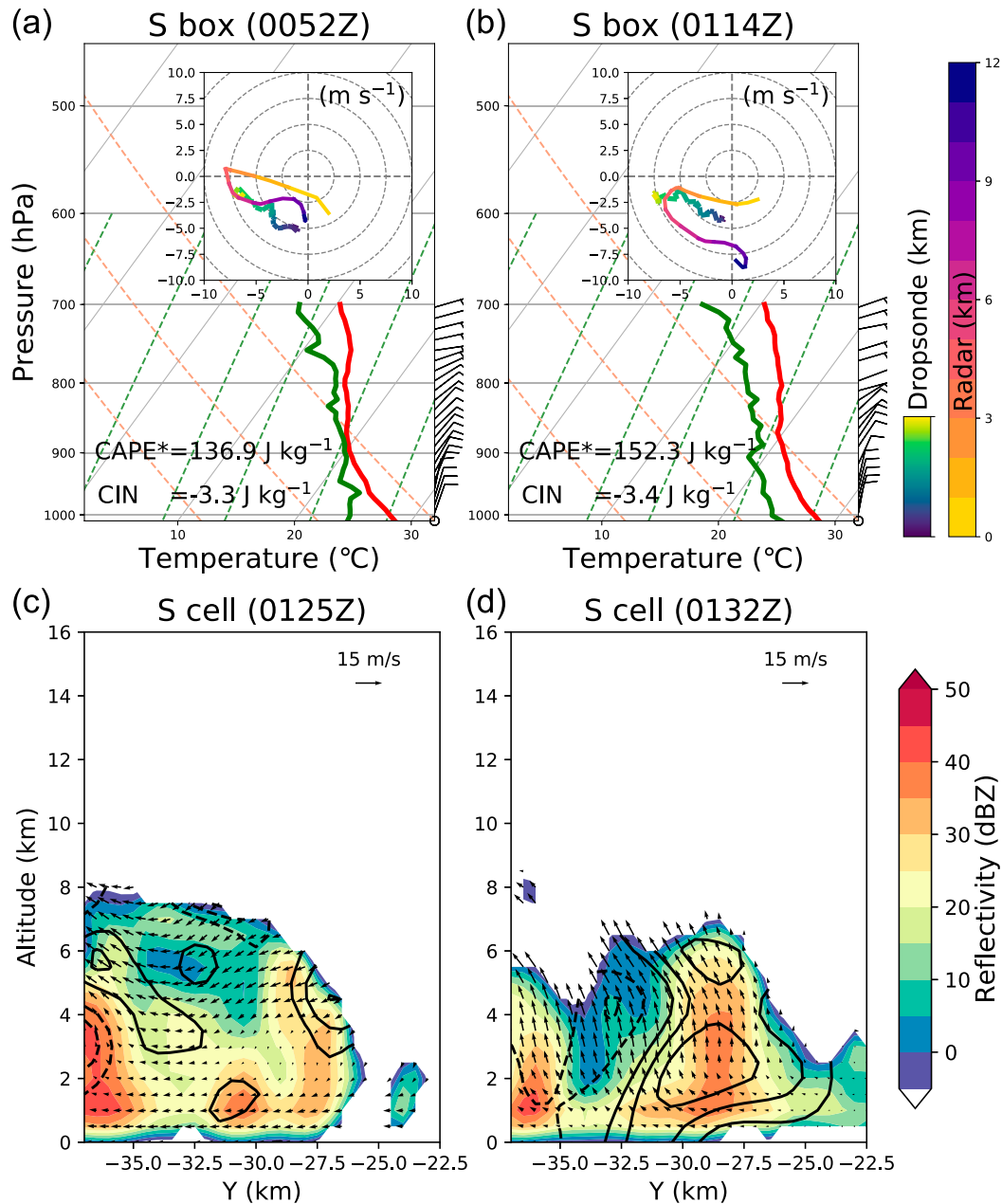
FIG. 12. As in Fig. 11, but in the S box. The radar hodograph is based on wind retrieved from dual-Doppler radar at (a) 0051–0058 and (b) 0128–0140 UTC averaged over the S box, and the vertical cross sections are at (c) 0125 and (b) 0132 UTC. The S-cell cross section is taken along $X = -32.5$ km in Fig. 8d.

two new categories to the framework based on South China Sea Monsoon Experiment (SCSMEX). In the N box, the mature N–S linear convection agrees with the convective structure mode with large northerly midlevel shear and small low-level shear [category 3 of LeMone et al. (1998)].[2] In the S box, the

characteristic and orientation of the squall-line like convection is consistent with the convective structure mode under strong low-level shear and weak midlevel shear [category 2r of Johnson et al. (2005)]. This mode is characterized with dry air aloft with linear organization parallel to the low-level shear vector and relatively short (~7-km echo top) and weak (maximum below 40 dBZ) reflectivity. The geometry of the situation suggests that in general for a wave pouch carried by an easterly wave, the low-level shear should be the largest to the south of the LLC center and the smallest to the north. In general, easterly waves have

----

[2] Note the difference between midlevel shear definition of our study (800–500 hPa) and that of LeMone et al. (1998) and Johnson et al. (2005) (800–400 hPa).
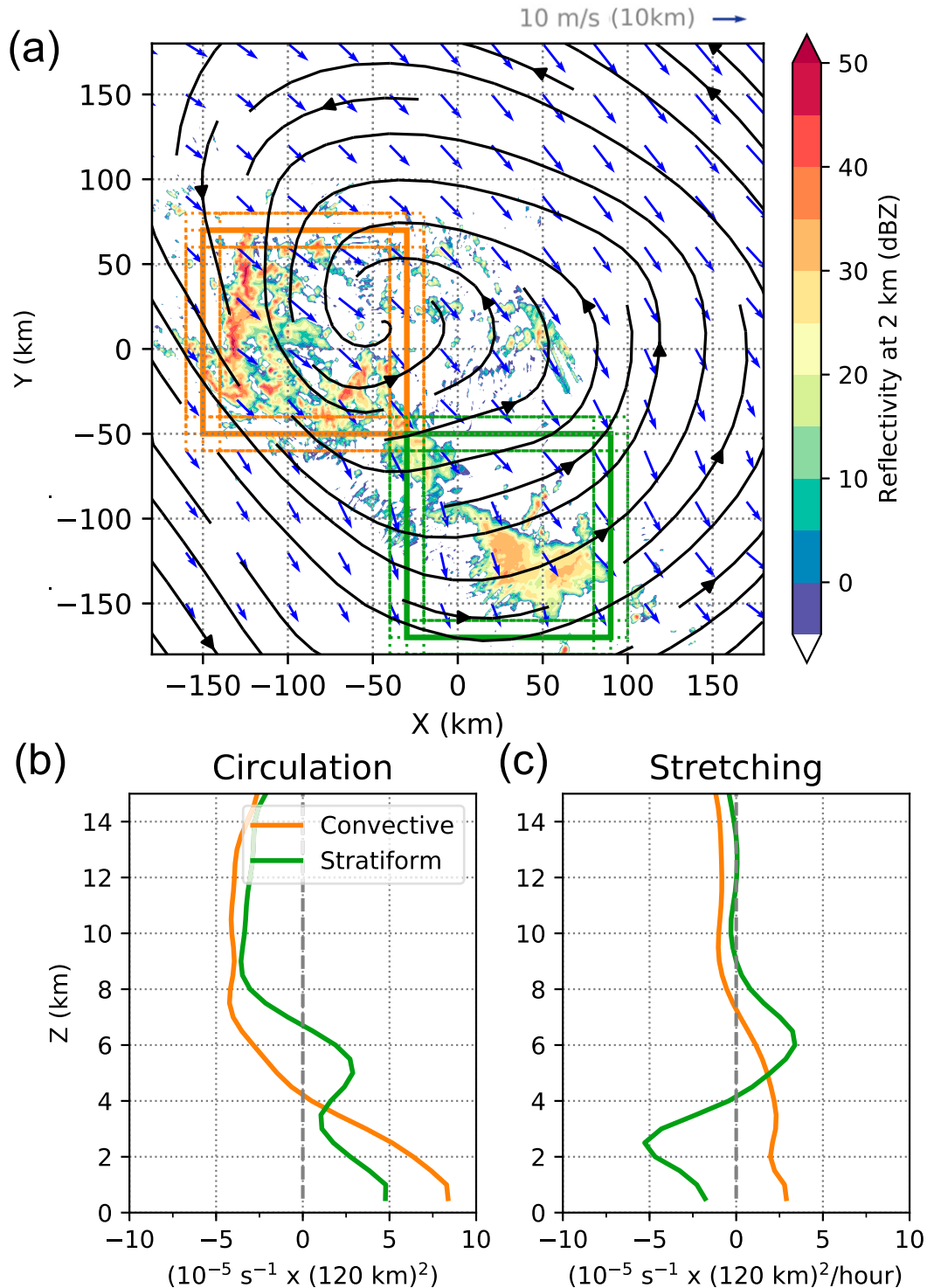
FIG. 13. Meso-α-scale structure of predepression Hagupit at 0000 UTC 14 Sep: (a) radar reflectivity at 2 km (shading) with wave-relative streamlines at 1 km (black) and wind vectors at 10 km (blue). Orange- and green-outlined boxes are 120 km × 120 km encompassing regions of primarily convective and stratiform precipitation in the pouch, respectively. The dotted lines indicate nine ensemble boxes shifted for (−10, 0, 10 km) in the x and y directions. Also shown are the (b) circulation and (c) stretching tendency with height. Orange and green lines are averaged over the nine dotted orange and green boxes in (a).
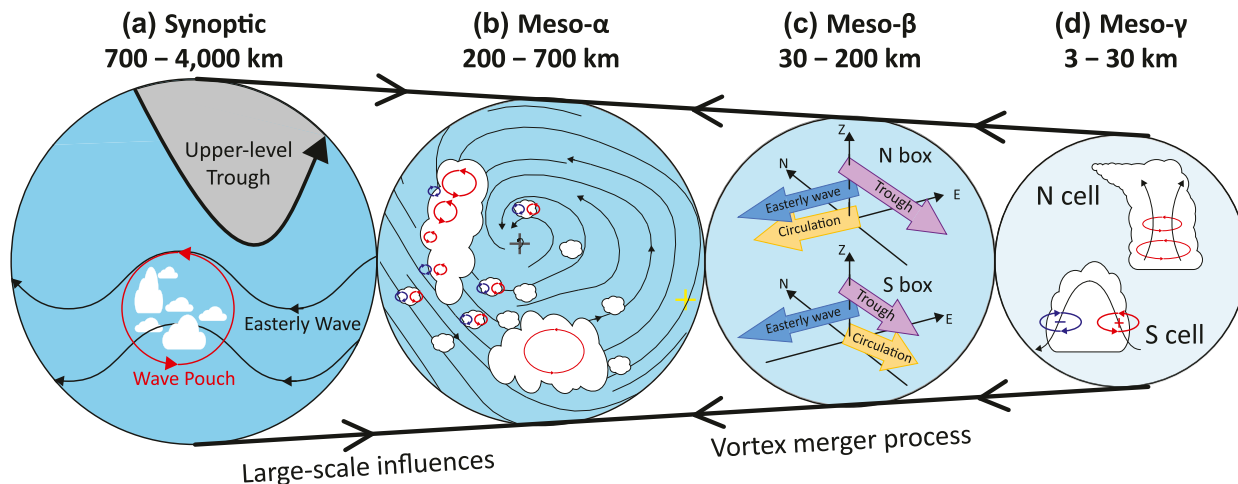
FIG. 14. Schematic of the multiscale interactions in Hagupit's cyclogenesis: (a) Synoptic-scale active features are the upper-level trough and easterly wave that carries the marsupial wave pouch, denoted as red circulation. (b) In the meso-α-scale wave pouch, the low-level cyclonic streamlines are shown with the circulation center marked with a black cross and the midlevel center marked with a yellow cross. Overlaid on the clouds to the southwest of the low-level center is vorticity (positive: red, negative: blue), illustrating vorticity dipoles from tilting, enhanced vorticity from stretching, and a midlevel MCV over the stratiform area. (c) In the meso-β scale, the local wind shear profile that influences the convective organization comprises winds from cyclonic circulation inside the pouch, easterly wave propagation, and the trough. (d) Meso-γ-scale convective cells produce vorticity that serves as building blocks for the wave-pouch intensification through tilting of horizontal vorticity associated with low-level wind shear (S cell) and stretching of the local vertical vorticity (N cell). See the text for a description of each physical process.

maximum easterly winds at 700–850 hPa (Serra et al. 2008), and with the cyclonic circulation near surface, westerlies can be found to the south of the LLC center and easterlies to the north. Whether the arrangement of low-level shear and organization of convection with respect to the LLC and the marsupial wave can be generalized to other tropical cyclogenesis cases beyond Hagupit is an interesting topic for future research. We note that the low-level shear organizes convection, but that convective processes such as cold pools can affect shear profiles in turn. Given the consistent low-level shear profile for a 30-min period in both the N box and the S box (Figs. 11 and 12), we believe the shear profiles in the meso-β scale are largely controlled by the downscale processes from synoptic and meso-α scales.

In the meso-γ-scale circle (Fig. 14d), vortical convection is illustrated. The convective cells are the building blocks for the predepression intensification. The wave pouch protects the convective cells from environmental dry air induced by the upper-level trough. Then the convective cells, in turn, enhance the circulation by generating and amplifying vertical vorticity. In the S box, where low-level shear was much stronger than in the N box, the convective cells (e.g., S cell) had larger values of the tilting term in the low levels. Congestus clouds like the S cell can provide initial vertical vorticity by tilting the horizontal vortex tube. The importance of low-level shear and tilting in the incipient tropical disturbance prior to genesis was also emphasized by Davis (2015). In the weak cyclonic environment of the predepression, tilting by cumulus congestus can play a major role providing the initial vertical vorticity to stretch. Tilting alone cannot contribute to net increase of vorticity in the wave pouch as long as the wave pouch fully encompasses both cyclonic and anticyclonic parts of vorticity dipoles generated by

tilting. However, the cyclonic part of the dipole can be stretched by the maturing convective cell (Hendricks et al. 2004; Montgomery et al. 2006). Then, stretching can produce a net positive vorticity generation in meso-γ scale, which can feed up to meso-α scale (Fig. 13c).

Recent observational studies have found that higher midlevel humidity is one of the most distinctive differences between developing and nondeveloping disturbances (Montgomery et al. 2012; Davis and Ahijevych 2013; Komaromi 2013; Zawislak and Zipser 2014). Despite the evident vortex misalignment at midlevels, Hagupit's low-level recirculating pouch was apparently able to continue providing moisture above the boundary layer (Fig. 5b). The closed low-level pouch protected the developing disturbance from nearby dry air intrusions. Then the convective clouds initiated from the low-level (especially convective congestus) moisten the midtroposphere above the boundary layer through vertical moisture flux (Wang 2014). The continuous moistening inside the wave pouch evident in reanalysis (Fig. 6) suggests that the convection on 14 September was able to sufficiently maintain the predepression. It is noteworthy that Hagupit had a favorable sea surface temperature throughout its pregenesis-to-genesis period above 30°C that supported strong surface moisture flux.

Hagupit intensified into a TD only after it had a midlevel vortex above the low-level circulation. The rapid increase in cold cloud coverage over the wave-pouch area was correlated with the midlevel vorticity intensification around 0000 UTC 18 September (Figs. 6e,f). Previous studies have shown that midlevel vortex can spin up through the convective processes, including vertical vorticity advection from deep convection (e.g., Chen et al. 2018) and midlevel stretching associated with

ice processes from stratiform precipitation (e.g., Bell and Montgomery 2019). Our ability to explain the later period of Hagupit's genesis on 16–19 September is limited because we do not have high resolution radar observation for this period, but we hypothesize that the feedback of water vapor, convection, and circulation in the early stage of Hagupit's tropical cyclogenesis during 13–15 September allowed for the subsequent genesis process of vortex realignment and precipitation symmetrization after Hagupit escaped from the upper-level trough and strong VWS (Rios-Berrios et al. 2018; Chen et al. 2018).

This case study provides a detailed observational analysis of multiscale processes around an incipient wave pouch surviving through strong VWS. Further observational and modeling studies are needed to investigate the complex processes across spatial scales during tropical cyclogenesis, especially in sheared environments. The roles of localized low-level shear and cumulus congestus clouds inside the wave pouch at the early stage of tropical cyclogenesis in particular warrant further exploration.

REFERENCES

Aiyyer, A., Z. Wang, R. McTaggart-Cowan, and S. K. R. Bhowmik, 2014: Cyclogenesis. WMO Doc., 13 pp., https://www.wmo.int/pages/prog/arep/wwrp/new/documents/IWTC_VIII_Topic2_1_Cyclogenesis_Final.pdf.

Bell, M. M., and M. T. Montgomery, 2010: Sheared deep vortical convection in pre-depression Hagupit during TCS08. *Geophys. Res. Lett.*, **37**, L06802, https://doi.org/10.1029/2009GL042313.

——, and ——, 2019: Mesoscale processes during the genesis of Hurricane Karl (2010). *J. Atmos. Sci.*, **76**, 2235–2255, https://doi.org/10.1175/JAS-D-18-0161.1.

——, ——, and K. A. Emanuel, 2012: Air–sea enthalpy and momentum exchange at major hurricane wind speeds observed during CBLAST. *J. Atmos. Sci.*, **69**, 3197–3222, https://doi.org/10.1175/JAS-D-11-0276.1.

Chang, M., C.-H. Ho, J. C. L. Chan, M.-S. Park, S.-W. Son, and J. Kim, 2019: The tropical transition in the western North Pacific: The case of Tropical Cyclone Peipah (2007). *J. Geophys. Res. Atmos.*, **124**, 5151–5165, https://doi.org/10.1029/2018JD029446.

Chen, X., Y. Wang, J. Fang, and M. Xue, 2018: A numerical study on rapid intensification of Typhoon Vicente (2012) in the South China Sea. Part II: Roles of inner-core processes. *J. Atmos. Sci.*, **75**, 235–255, https://doi.org/10.1175/JAS-D-17-0129.1.

Corbosiero, K. L., and J. Molinari, 2002: The effects of vertical wind shear on the distribution of convection in tropical cyclones. *Mon. Wea. Rev.*, **130**, 2110–2123, https://doi.org/10.1175/1520-0493(2002)130<2110:TEOVWS>2.0.CO;2.

Davis, C. A., 2015: The formation of moist vortices and tropical cyclones in idealized simulations. *J. Atmos. Sci.*, **72**, 3499–3516, https://doi.org/10.1175/JAS-D-15-0027.1.

——, and L. F. Bosart, 2003: Baroclinically induced tropical cyclogenesis. *Mon. Wea. Rev.*, **131**, 2730–2747, https://doi.org/10.1175/1520-0493(2003)131<2730:BITC>2.0.CO;2.

——, and T. J. Galarneau, 2009: The vertical structure of mesoscale convective vortices. *J. Atmos. Sci.*, **66**, 686–704, https://doi.org/10.1175/2008JAS2819.1.

——, and D. A. Ahijevych, 2013: Thermodynamic environments of deep convection in Atlantic tropical disturbances. *J. Atmos. Sci.*, **70**, 1912–1928, https://doi.org/10.1175/JAS-D-12-0278.1.

DeHart, J. C., J. Houze, A. Robert, and R. F. Rogers, 2014: Quadrant distribution of tropical cyclone inner-core kinematics in relation to environmental shear. *J. Atmos. Sci.*, **71**, 2713–2732, https://doi.org/10.1175/JAS-D-13-0298.1.

Dunkerton, T. J., M. T. Montgomery, and Z. Wang, 2009: Tropical cyclogenesis in a tropical wave critical layer: Easterly waves. *Atmos. Chem. Phys.*, **9**, 5587–5646, https://doi.org/10.5194/acp-9-5587-2009.

Elsberry, R. L., and P. A. Harr, 2008: Tropical Cyclone Structure (TCS08) field experiment science basis, observational platforms, and strategy. *Asia-Pac. J. Atmos. Sci.*, **44**, 209–231.

Fang, J., and F. Zhang, 2011: Evolution of multiscale vortices in the development of Hurricane Dolly (2008). *J. Atmos. Sci.*, **68**, 103–122, https://doi.org/10.1175/2010JAS3522.1.

Finocchio, P. M., S. J. Majumdar, D. S. Nolan, and M. Iskandarani, 2016: Idealized tropical cyclone responses to the height and depth of environmental vertical wind shear. *Mon. Wea. Rev.*, **144**, 2155–2175, https://doi.org/10.1175/MWR-D-15-0320.1.

Fischer, M. S., B. H. Tang, and K. L. Corbosiero, 2019: A climatological analysis of tropical cyclone rapid intensification in environments of upper-tropospheric troughs. *Mon. Wea. Rev.*, **147**, 3693–3719, https://doi.org/10.1175/MWR-D-19-0013.1.

Foerster, A. M., M. M. Bell, P. A. Harr, and S. C. Jones, 2014: Observations of the eyewall structure of Typhoon Sinlaku (2008) during the transformation stage of extratropical transition. *Mon. Wea. Rev.*, **142**, 3372–3392, https://doi.org/10.1175/MWR-D-13-00313.1.

Hendricks, E. A., M. T. Montgomery, and C. A. Davis, 2004: The role of "vertical" hot towers in the formation of Tropical Cyclone Diana (1984). *J. Atmos. Sci.*, **61**, 1209–1232, https://doi.org/10.1175/1520-0469(2004)061<1209:TROVHT>2.0.CO;2.

Holton, J., 2004: *An Introduction to Dynamic Meteorology.* Elsevier Science, 535 pp.

Houze, R. A., Jr., 2004: Mesoscale convective systems. *Rev. Geophys.*, **42**, RG4003, https://doi.org/10.1029/2004RG000150.

Johnson, R. H., T. M. Rickenbach, S. A. Rutledge, P. E. Ciesielski, and W. H. Schubert, 1999: Trimodal characteristics of tropical convection. *J. Climate*, **12**, 2397–2418, https://doi.org/10.1175/1520-0442(1999)012<2397:TCOTC>2.0.CO;2.

——, S. L. Aves, P. E. Ciesielski, and T. D. Keenan, 2005: Organization of oceanic convection during the onset of the 1998 East Asian summer monsoon. *Mon. Wea. Rev.*, **133**, 131–148, https://doi.org/10.1175/MWR-2843.1.

Jones, S. C., 1995: The evolution of vortices in vertical shear. I: Initially barotropic vortices. *Quart. J. Roy. Meteor. Soc.*, **121**, 821–851, https://doi.org/10.1002/qj.49712152406.

Kilroy, G., R. K. Smith, and U. Wissmeier, 2014: Tropical convection: The effects of ambient vertical and horizontal vorticity. *Quart. J. Roy. Meteor. Soc.*, **140**, 1756–1770, https://doi.org/10.1002/qj.2261.

Knapp, K. R., 2014: NOAA climate data record (CDR) of gridded satellite data from ISCCP B1 (GridSat-B1) infrared channel brightness temperature, version 2. NOAA CDR Program, accessed 13 September 2020, https://doi.org/10.7289/V59P2ZKR.

Komaromi, W. A., 2013: An investigation of composite dropsonde profiles for developing and nondeveloping tropical waves during the 2010 PREDICT field campaign. *J. Atmos. Sci.*, **70**, 542–558, https://doi.org/10.1175/JAS-D-12-052.1.

LeMone, M. A., E. J. Zipser, and S. B. Trier, 1998: The role of environmental shear and thermodynamic conditions in determining the structure and evolution of mesoscale convective systems during TOGA COARE. *J. Atmos. Sci.*, **55**, 3493–3518, https://doi.org/10.1175/1520-0469(1998)055<3493:TROESA>2.0.CO;2.

McTaggart-Cowan, R., J. Galarneau, J. Thomas, L. F. Bosart, R. W. Moore, and O. Martius, 2013: A global climatology of baroclinically influenced tropical cyclogenesis. *Mon. Wea. Rev.*, **141**, 1963–1989, https://doi.org/10.1175/MWR-D-12-00186.1.

Molinari, J., P. Dodge, D. Vollaro, K. L. Corbosiero, and F. Marks, 2006: Mesoscale aspects of the downshear reformation of a tropical cyclone. *J. Atmos. Sci.*, **63**, 341–354, https://doi.org/10.1175/JAS3591.1.

Montgomery, M. T., M. E. Nicholls, T. A. Cram, and A. B. Saunders, 2006: A vortical hot tower route to tropical cyclogenesis. *J. Atmos. Sci.*, **63**, 355–386, https://doi.org/10.1175/JAS3604.1.

——, and Coauthors, 2012: The Pre-Depression Investigation of Cloud-Systems in the Tropics (PREDICT) experiment: Scientific basis, new analysis tools, and some first results. *Bull. Amer. Meteor. Soc.*, **93**, 153–172, https://doi.org/10.1175/BAMS-D-11-00046.1.

Nguyen, L. T., and J. Molinari, 2015: Simulation of the downshear reformation of a tropical cyclone. *J. Atmos. Sci.*, **72**, 4529–4551, https://doi.org/10.1175/JAS-D-15-0036.1.

Nolan, D., and M. McGauley, 2012: Tropical cyclogenesis in wind shear: Climatological relationships and physical processes. *Cyclones: Formation, Triggers and Control*, H. Fudeyasu and K. Oouchi, Eds., Nova Science Publishers, 1–36.

Ooyama, K., 1969: Numerical simulation of the life cycle of tropical cyclones. *J. Atmos. Sci.*, **26**, 3–40, https://doi.org/10.1175/1520-0469(1969)026<0003:NSOTLC>2.0.CO;2.

Pendergrass, A. G., and H. E. Willoughby, 2009: Diabatically induced secondary flows in tropical cyclones. Part I: Quasi-steady forcing. *Mon. Wea. Rev.*, **137**, 805–821, https://doi.org/10.1175/2008MWR2657.1.

Pytharoulis, I., and C. Thorncroft, 1999: The low-level structure of African easterly waves in 1995. *Mon. Wea. Rev.*, **127**, 2266–2280, https://doi.org/10.1175/1520-0493(1999)127<2266:TLLSOA>2.0.CO;2.

Raymond, D. J., and S. L. Sessions, 2014: Tropical cyclogenesis and mid-level vorticity. *Aust. Meteor. Oceanogr. J.*, **64**, 11–25, https://doi.org/10.22499/2.6401.003.

——, C. López-Carrillo, and L. L. Cavazos, 1998: Case-studies of developing east Pacific easterly waves. *Quart. J. Roy. Meteor. Soc.*, **124**, 2005–2034, https://doi.org/10.1002/qj.49712455011.

——, and H. Jiang, 1990: A theory for long-lived mesoscale convective systems. *J. Atmos. Sci.*, **47**, 3067–3077, https://doi.org/10.1175/1520-0469(1990)047<3067:ATFLLM>2.0.CO;2.

Reasor, P. D., and M. T. Montgomery, 2015: Evaluation of a heuristic model for tropical cyclone resilience. *J. Atmos. Sci.*, **72**, 1765–1782, https://doi.org/10.1175/JAS-D-14-0318.1.

——, ——, and L. D. Grasso, 2004: A new look at the problem of tropical cyclones in vertical shear flow: Vortex resiliency. *J. Atmos. Sci.*, **61**, 3–22, https://doi.org/10.1175/1520-0469(2004)061<0003:ANLATP>2.0.CO;2.

Reed, R. J., and E. E. Recker, 1971: Structure and properties of synoptic-scale wave disturbances in the equatorial western Pacific. *J. Atmos. Sci.*, **28**, 1117–1133, https://doi.org/10.1175/1520-0469(1971)028<1117:SAPOSS>2.0.CO;2.

Rienecker, M., and Coauthors, 2008: The GEOS-5 Data Assimilation System—Documentation of versions 5.0.1, 5.1.0, and 5.2.0. NASA Tech. Memo. NASA/TM-2008-104606, Vol. 27, 97 pp., http://gmao.gsfc.nasa.gov/pubs/docs/Rienecker369.pdf.

Rios-Berrios, R., and R. D. Torn, 2017: Climatological analysis of tropical cyclone intensity changes under moderate vertical wind shear. *Mon. Wea. Rev.*, **145**, 1717–1738, https://doi.org/10.1175/MWR-D-16-0350.1.

——, C. A. Davis, and R. D. Torn, 2018: A hypothesis for the intensification of tropical cyclones under moderate vertical wind shear. *J. Atmos. Sci.*, **75**, 4149–4173, https://doi.org/10.1175/JAS-D-18-0070.1.

Serra, Y. L., G. N. Kiladis, and M. F. Cronin, 2008: Horizontal and vertical structure of easterly waves in the Pacific ITCZ. *J. Atmos. Sci.*, **65**, 1266–1284, https://doi.org/10.1175/2007JAS2341.1.

Tang, B., and K. Emanuel, 2010: Midlevel ventilation's constraint on tropical cyclone intensity. *J. Atmos. Sci.*, **67**, 1817–1830, https://doi.org/10.1175/2010JAS3318.1.

——, and ——, 2012: Sensitivity of tropical cyclone intensity to ventilation in an axisymmetric model. *J. Atmos. Sci.*, **69**, 2394–2413, https://doi.org/10.1175/JAS-D-11-0232.1.

Tao, D., and F. Zhang, 2014: Effect of environmental shear, sea-surface temperature, and ambient moisture on the formation and predictability of tropical cyclones: An ensemble-mean perspective. *J. Adv. Model. Earth Syst.*, **6**, 384–404, https://doi.org/10.1002/2014MS000314.

Van Sang, N., R. K. Smith, and M. T. Montgomery, 2008: Tropical-cyclone intensification and predictability in three dimensions. *Quart. J. Roy. Meteor. Soc.*, **134**, 563–582, https://doi.org/10.1002/qj.235.

Vigh, J. L., and W. H. Schubert, 2009: Rapid development of the tropical cyclone warm core. *J. Atmos. Sci.*, **66**, 3335–3350, https://doi.org/10.1175/2009JAS3092.1.

Wang, Z., 2012: Thermodynamic aspects of tropical cyclone formation. *J. Atmos. Sci.*, **69**, 2433–2451, https://doi.org/10.1175/JAS-D-11-0298.1.

——, 2014: Role of cumulus congestus in tropical cyclone formation in a high-resolution numerical model simulation. *J. Atmos. Sci.*, **71**, 1681–1700, https://doi.org/10.1175/JAS-D-13-0257.1.

——, M. T. Montgomery, and T. J. Dunkerton, 2010: Genesis of pre–Hurricane Felix (2007). Part I: The role of the easterly wave critical layer. *J. Atmos. Sci.*, **67**, 1711–1729, https://doi.org/10.1175/2009JAS3420.1.

Weightman, R. H., 1919: The west India hurricane of September, 1919, in the light of sounding observations. *Mon. Wea. Rev.*, **47**, 717–721, https://doi.org/10.1175/1520-0493(1919)47<717:TWIHOS>2.0.CO;2.

Wissmeier, U., and R. K. Smith, 2011: Tropical cyclone convection: The effects of ambient vertical vorticity. *Quart. J. Roy. Meteor. Soc.*, **137**, 845–857, https://doi.org/10.1002/qj.819.

Zawislak, J., and E. J. Zipser, 2014: Analysis of the thermodynamic properties of developing and nondeveloping tropical disturbances using a comprehensive dropsonde dataset. *Mon. Wea. Rev.*, **142**, 1250–1264, https://doi.org/10.1175/MWR-D-13-00253.1.

Zehr, R. M., 1992: Tropical cyclogenesis in the western North Pacific. NOAA Tech. Rep. NESDIS 61, 181 pp., https://repository.library.noaa.gov/view/noaa/13116/noaa_13116_DS1.pdf.